Journal of Biomedicine and Biosensors, 6(3):9–24, Jul-Sep: 2026.
DOI: https://doi.org/10.58613/jbb632

Journal of Biomedicine and Biosensors
ISSN (Online): 2583-3170

Journal homepage: https://gpub.org/journal-details.php?journal-id=45

Research Article

Pelargonidin-Strontium Oxide Nanoparticles: Enhanced Targeted Therapy for Triple-Negative Breast Cancer

Peng Zhang[1], Chao Wang[1], Mengmeng Qi[1], Qian Hu[1], Wenwen Liu[1] and Ying Zhang[1*]

[1] *Department of Breast Surgery, Affiliated Hospital of Hebei University, Baoding, Hebei, China.*
[*] *Corresponding author: zhangying505015@sin.cn*

Article Info

Keywords: *Triple-negative breast cancer, Pelargonidin, Strontium oxide nanoparticles, Drug delivery, Apoptosis.*

Received: *06.06.2026;*
Accepted: *01.08.2026;*
Published: *12.08.2026*

Abstract

Triple-negative breast cancer (TNBC) is a highly aggressive neoplasm characterized by restricted therapeutic alternatives and a bleak prognosis. Nanotechnology-driven medication delivery methods improve therapeutic effectiveness while minimizing systemic toxicity. Pelargonidin (PL), a flavonoid with anticancer effects, has low absorption, hence limiting its therapeutic applicability. Strontium oxide (SrO) nanoparticles provide a viable platform for medication administration owing to their biocompatibility. This work included the synthesis of PL-SrO nanoparticles using co-precipitation, followed by characterization utilizing FTIR, XRD and TEM techniques. Drug release investigations demonstrated a pH-dependent release profile, with 85% of PL released at pH 6.5 (conditions simulating tumors) in contrast to 60% at pH 7.4 during a 24-hour period. *in vitro* tests shown that PL-SrO markedly decreased TNBC cell viability (IC_{50} = 2.8 μg/mL) in comparison to free PL (IC_{50} = 7.2 μg/mL), while showing no damage to normal cells. PL-SrO demonstrated superior inhibition of colony formation (90% decrease), migration (85% reduction), and invasion (90% reduction) compared to free PL. Apoptotic staining and mitochondrial membrane potential studies validated substantial activation of apoptosis. The formation of ROS increased by 350% with PL-SrO therapy, exceeding the impact of doxorubicin (DOX). Gene expression study demonstrated a 3.0-fold overexpression of BAX and a 2.8-fold rise in Caspase 9, accompanied by a 0.3-fold downregulation of BCL2 and BRCA1, indicating the activation of apoptosis and the suppression of DNA repair. The results indicate that PL-SrO nanoparticles improve PL bioavailability, specifically target TNBC cells, and trigger death via mitochondrial malfunction and oxidative stress, therefore underscoring their potential as a nanotherapeutic for TNBC.

1. Introduction

Triple-negative breast cancer (TNBC) is a notably aggressive kind of breast cancer, distinguished by the lack of certain receptor expressions. It constitutes around 15-20% of all worldwide breast cancer diagnoses, considerably impacting the total burden of the illness [1]. In 2020, over 2.3 million new breast cancer cases were identified globally, with TNBC constituting a significant fraction. This subtype accounts for a considerable number of yearly fatalities, with mortality rates persistently elevated in comparison to other breast cancer subtypes [1–3]. The incidence of TNBC in India is becoming problematic, particularly impacting younger women disproportionately. The five-year survival rate for this subtype is much lower than that of other breast cancer subtypes, mainly because of its aggressive characteristics, elevated metastatic potential, and restricted treatment alternatives [4, 5]. The etiology of TNBC is complex, including genetic predisposition, environmental

influences, and lifestyle decisions. Contemporary therapeutic approaches, including surgery, chemotherapy, and radiation, often encounter obstacles owing to drug resistance, systemic toxicity, and the absence of tailored medicines, underscoring the pressing need for innovative and efficacious treatment methods [6–8].

Nanotechnology offers a viable approach to transform cancer therapy through tailored medication delivery, improved bioavailability, and less systemic toxicity. The capacity to accurately administer therapeutic drugs to tumor locations while reducing off-target effects is essential for enhancing therapy effectiveness and patient outcomes [9–11]. Researchers are investigating natural chemicals with anticancer characteristics, including pelargonidin (PL), a flavonoid present in different berries, fruits, and flowers, including strawberries and raspberries [12, 13]. PL demonstrates several therapeutic advantages, including antioxidant, anti-inflammatory, and anticancer properties [14–18]. Nonetheless, its clinical use is limited by inadequate solubility, fast metabolism, and diminished bioavailability. Encapsulating PL in nanoparticles might mitigate these limitations, augmenting its stability, solubility, and targeted transport to cancer cells, thereby boosting its therapeutic effectiveness [19–22].

Strontium oxide (SrO) nanoparticles have been a prominent area of interest in biomedical applications, especially in cancer treatment, due to their intrinsic biocompatibility, non-toxicity, and capability for regulated drug administration. SrO has osteogenic characteristics and has been thoroughly investigated for use in bone tissue engineering and medication administration. In addition to its usefulness in bone, SrO's distinctive properties make it a good candidate for cancer therapy. The alkaline properties may facilitate intracellular pH regulation, potentially augmenting the effectiveness of certain anticancer agents by altering the tumor microenvironment and enhancing drug absorption. Moreover, SrO's biocompatibility guarantees minimum detrimental effects on healthy tissues, while its biodegradability facilitates slow disintegration and expulsion from the body. Significantly, SrO nanoparticles may augment the bioavailability of therapeutic drugs, promoting effective transport to tumor locations [23–31].

We aim to synthesize PL-encapsulated SrO (PL-SrO) nanoparticles using co-precipitation, describe their physicochemical attributes and assess their *in vitro* anticancer effectiveness against triple-negative breast cancer cells. Evaluate drug release kinetics, cell proliferation, colony formation, biocompatibility, migration, invasion, cellular uptake, apoptosis, reactive oxygen species production, mitochondrial membrane potential disturbance, and alterations in gene expression. These *in vitro* experiments will be evaluated against the traditional chemotherapeutic agent, doxorubicin (DOX), which, while efficacious, is linked to considerable drawbacks such as systemic toxicity and drug resistance [32–34]. We propose that PL-SrO nanoformulation will exhibit enhanced anticancer efficacy and less toxicity relative to DOX, presenting a viable treatment approach for triple-negative breast cancer.

2. Methods

2.1. Synthesis of PL-SrO

The PL-SrO nanoformulation was produced using a co-precipitation technique [35–38]. In brief, 50 mL of a 0.1 M strontium chloride ($SrCl_2$) precursor solution was generated, and 10 mL of a 0.01 M PL solution was gradually added to the $SrCl_2$ solution while maintaining steady magnetic stirring at 500 rpm, preserving a 10:1 molar ratio of Sr^{2+} to PL. Subsequently, a 1 M NaOH solution was incrementally added at a rate of 1 mL/minute to the mixture, facilitating the co-precipitation of SrO in the presence of PL while maintaining a pH of 11. The resultant precipitate was agitated at 500 rpm for one hour, followed by 24 hours at ambient temperature to improve crystallinity. The precipitate was further isolated using centrifugation at 8000 rpm for 10 minutes, meticulously rinsed three times with 50 mL of deionized water and once with 50 mL of ethanol to eliminate residual ions, and ultimately dried under vacuum at 60°C for 24 hours to provide the PL-SrO nanopowder for subsequent applications.

The nanoparticle suspension is subjected to ultracentrifugation to ascertain PL entrapment. The supernatant, which contains free PL, and the resuspended nanoparticle pellet, which contains encapsulated PL were evaluated using UV-Vis spectrophotometry at 524 nm. Entrapment efficiency (EE) is determined as the proportion of the entire PL originally used that is present inside the nanoparticle pellet.

2.2. Characterization of PL-SrO

Functional group identification was conducted using FTIR spectroscopy, utilizing the KBr pellet method for sample preparation and acquiring spectra in the range of 400 to 4000 cm^{-1} with a Shimadzu FTIR. The cryastalline phase and structural parameters were ascertained using XRD employing with Cu Kα radiation, capturing diffraction patterns within the 10° to 70° range. The morphology of the nanocomposites was examined using TEM, with diluted samples deposited on carbon-coated copper grids and photographed using a Zeiss.

2.3. Drug releasing analysis

We examined the *in vitro* release of PL from SrO nanoparticles using dialysis membranes, emphasizing the influence of pH. 2 mg of PL-SrO nanoparticles were enclosed in dialysis bags (14 KDa) and immersed in PBS solutions at pH levels of 7.4 and 6.5 [39]. The solutions were stirred at 37°C. Hourly samples of 1 mL were collected during 24 hours of incubation, and the released PL was quantified using UV-Vis spectroscopy at 525 nm. The findings enabled a comparison of PL release at two pH levels, elucidating the nanoparticle's activity under varying physiological stages.

2.4. Cell maintenance

TNBC cell lines (MDA-MB-231) and non-cancerous breast epithelial cell lines (MC7- 10A) were maintained in the DMEM with 10% FBS and 1% antibiotics at 5% CO_2 and 37°C.

Cell proliferation assay

The cytotoxic effects of DOX, PL, and SrO-PL nanoparticles on MDA-MB-231 and MCF-10A cell lines were assessed by seeding cells (1×10^4/well) in 96-well plates and treating them with different doses (0.2, 1, 2, 4, 6, and 8 μg/mL) of each chemical for 24 hours. Cell viability was assessed by the MTT test, which included measuring the spectrophotometric conversion of MTT to formazan by viable cells at 575 nm [39]. Cell viability was assessed in untreated control cells, and dose-response curves were made to get IC_{50} values.

Cellular uptake assay

A fluorescence microscopy-based assay was conducted to visualize and quantify the cellular uptake of nanoparticles. To visualize intracellular uptake, DOX, PL, and PL-SrO nanoparticles were conjugated with FITC using standard amine coupling protocols. This facilitated direct fluorescence tracking of nanoparticles within cells. Before treatment, cells were seeded and incubated until an appropriate confluency was achieved. Cells were subsequently exposed to FITC-labeled DOX, PL, and PL-SrO nanoparticles at their respective IC_{50} concentrations for a period of 2 to 4 hours at 37°C in a 5% CO_2 environment. After incubation, cells were fixed using 4% paraformaldehyde to maintain cellular structure. Fluorescence imaging was performed utilizing a 100 × objective with suitable excitation and emission filters for FITC (488/525 nm) [40]. The analysis of acquired images was conducted using ImageJ software, which quantified fluorescence intensity within individual cells and mapped the intracellular distribution of nanoparticles, thereby elucidating their uptake mechanisms.

Colony formation assay

A colony formation assay was performed to evaluate the long-term proliferative capacity of TNBC cells following treatment with DOX, PL, and PL-SrO nanoparticles. Cells were cultured at a density of 500 cells per well and exposed to various concentrations of the compounds, including their respective IC_{50} values. Colonies were fixed after 10 days, stained with Giemsa solution, and subsequently quantified using ImageJ software [40, 41].

Migration assay

A scratch wound healing assay was performed to evaluate the effect of nanoparticles on the migration ability of MDA-MB-231 cells. TNBC cells were cultured to 80% confluency in culture plates. A linear scratch was created in the cell monolayer using a sterile 200 μL pipette tip [42]. Following treatment with the compounds and their respective IC_{50} values, the closure of the scratch wound was observed and recorded over 24 hours. The extent of wound closure was quantified by the residual gap width using ImageJ analysis software, providing an evaluation of the compounds' effectiveness in suppressing cancer cell migration.

Invasion assay

A Matrigel-coated transwell insert invasion assay was performed to assess the effect of nanoparticles on the invasive potential of TNBC cells. The cells were positioned in the upper chamber of the Matrigel-coated insert, whereas the lower chamber held a culture medium. Following a 24-hour treatment with the compounds, including their IC_{50} values, cells that invaded through the Matrigel and migrated to the lower surface of the membrane were fixed, stained, and quantified [43]. The number of invaded cells was evaluated using ImageJ software, providing a measure of the compounds' effectiveness in preventing cancer cell invasion.

Apoptotic staining

To assess the induction of apoptosis in TNBC cells after nanoparticle treatment, an AO/EtBr staining assay was conducted. Cells (1×10^4) were cultured and exposed to the compounds for 24 hours. Post-treatment, cells were collected, rinsed with PBS, and subsequently stained with a combination of AO/EtBr (10 μg/mL) for 5 minutes in the dark. Stained cells were subsequently visualized using a fluorescent microscope at 100 × magnification [41].

MMP level analysis

A rhodamine 123 (RhO) staining assay was conducted to evaluate the effect of synthesized nanoparticles on MMP in TNBC cells. Cells (1×10^4) were seeded and treated with the compounds, along with their respective IC_{50} values, for 24 hours. Post-treatment, cells were rinsed with PBS and incubated with RhO (10 μg/mL) for 20 minutes at 37°C in the absence of light. Rhodamine 123 accumulates in mitochondria that maintain an intact membrane potential, leading to green fluorescence. Cells were subsequently washed to eliminate unbound dye and were immediately analyzed using a fluorescent microscope at 100 × magnification (488/530).

ROS estimation

A DCFH-DA assay was conducted to assess the generation of ROS in TNBC cells after treatment with nanoparticles. Cells were seeded at a density of (1×10^4) and treated with the compounds, along with their respective IC_{50} values, for 24 hours. Following treatment, cells were rinsed with PBS and incubated with DCFH-DA (10 μM) for 25 minutes at 37°C in the absence of light. DCFH-DA is a non-fluorescent compound that, upon cellular entry, undergoes deacetylation by esterases and oxidation by ROS, resulting in the formation of fluorescent DCF. Cells were subsequently washed to eliminate unbound dye and analyzed immediately using fluorescent microscopy with excitation at 488/525 nm.

Gene expression study

RT-qPCR was conducted to examine the molecular mechanisms of DOX, PL, and PL-SrO in TNBC cells. Total RNA isolation was performed with TRIzol reagent, followed by cDNA synthesis utilizing a [cDNA synthesis kit name]. Gene expression levels of BCL2, BAX, caspase, and BRCA1 were quantified utilizing gene-specific primers and SYBR Green Master Mix on a QuantStudio™ 5 Real-Time PCR System, with β-actin serving as an endogenous control. Relative mRNA levels were quantified as fold change $\pm$ SD in comparison to untreated controls.

2.5. Statistical analysis

Data are expressed as mean ± SEM, with a significance threshold set at $p < 0.05$. To determine statistical significance, a one-way ANOVA was used (GraphPad Prism 8).

3. Results and discussion

3.1. Co-precipitated PL-SrO nano formulation

The co-precipitation synthesis of PL-SrO nanoparticles represents an important advancement to achieve uniform nanoparticle formation and effective incorporation of PL. This accomplishment has its roots in the fundamental chemical structures of PL and SrO. PL, a polyhydroxylated anthocyanidin, contains multiple -OH groups and a comprehensive conjugated aromatic system, both critical for interacting with SrO. The co-precipitation process involves the reaction of (Sr^{2+} with an alkaline reagent, typically a NaOH solution, resulting in the nucleation of SrO [35]. The newly synthesized SrO nanoparticles, characterized by a surface rich in oxygen atoms and hydroxyl groups, provide multiple binding sites for pelargonidin molecules. The hydroxyl groups on pelargonidin facilitate hydrogen bond formation with the oxygen atoms and hydroxyl groups on the SrO surface. The polar characteristics of pelargonidin promote electrostatic interactions with positively charged Sr^{2+} ions, thereby improving its effective integration. The synthesis achieved an entrapment efficiency of 85.3% for PL within the SrO matrix. The high efficiency underscores the effectiveness of the co-precipitation method in facilitating the incorporation of the bioactive molecule. The co-precipitation method enables the swift formation of SrO in the presence of PL, improving the entrapment and surface adsorption of the bioactive molecule, which leads to a uniform distribution within the nanoparticle matrix.

3.2. FTIR

FTIR spectroscopy was utilized to identify the functional groups present in PL, and PL-SrO nanoparticles Figure 1a. The spectra exhibited distinct characteristic peaks for each sample, indicating the successful synthesis of SrO and the effective loading of PL onto the SrO matrix. The FTIR spectrum of pure PL exhibited a series of characteristic peaks. A prominent peak in the range of 3300-3400 cm^{-1} was identified, corresponding to the stretching vibrations of phenolic OH groups. Peaks at approximately 1640 cm^{-1} and 1520 cm^{-1} correspond to the stretching vibrations of the C=O and C=C bonds in the aromatic ring, respectively. Peaks within the 1000-1200 cm^{-1} range are indicative of C-O stretching vibrations [20, 44]. The FTIR spectrum of PL-SrO nanoparticles displayed a combination of peaks characteristic of both SrO and PL. The characteristic Sr-O stretching vibration was preserved, albeit with a slight reduction in intensity, suggesting an interaction between PL and the SrO surface. The peaks associated with the OH stretching and bending vibrations in SrO were observed, exhibiting variations in intensity and shape, indicating an interaction between PL molecules and surface OH groups. Peaks associated with the C=O and C=C stretching vibrations of PL were identified in the PL-SrO spectrum, thereby confirming the presence of PL in the nanocomposite. The peaks exhibited broadening and slight shifts, suggesting interactions between PL and SrO. The existence of surface hydroxyl groups on SrO, indicated by the peaks at 3400 cm^{-1} and 1630 cm^{-1}, is essential for the loading of PL. The FTIR analysis confirmed the successful formation of SrO nanoparticles and the efficient loading of PL.

3.3. XRD

XRD analysis was performed to determine the crystalline structure and phase composition of synthesized PL-SrO Figure 1b. The diffractogram of SrO nanoparticles displayed clear diffraction peaks at 2θ values of around 32.5°, 37.0°, 53.5°, 64.0°, and 67.5°, which correspond to the (111), (200), (220), (311), and (222) planes of the cubic phase of SrO (JCPDS card no. 06-0520) [45, 46]. The distinct characteristics of these peaks confirmed the successful formation of crystalline SrO nanoparticles exhibiting a cubic crystal structure, thereby validating the phase purity of the synthesized material. The observed broadening of these peaks aligns with nanoparticle formation, as smaller crystallite sizes inherently lead to broader diffraction peaks. The XRD pattern of the PL-SrO nanoparticles exhibited the retention of characteristic cubic SrO peaks, indicating that the incorporation of PL did not alter the fundamental crystal structure of SrO. A slight decrease in the intensity of the SrO peaks, accompanied by minor peak broadening, was observed. The observed changes are linked to the presence of PL on the surface and within the SrO matrix, potentially causing minor distortions in the SrO crystal lattice and disrupting long-range order. The lack of distinct pelargonidin peaks in the PL-SrO pattern indicates that the PL molecules are effectively dispersed within the SrO matrix, presumably in an amorphous state. The high dispersion inhibits the formation of distinct PL crystallites that would generate observable diffraction peaks, suggesting a uniform distribution of PL within the SrO nanoparticles. The XRD analysis confirmed the successful synthesis of crystalline SrO nanoparticles and the effective incorporation of PL in PL-SrO formulation.

3.4. TEM

Transmission electron microscopy (TEM) was employed to examine the structural morphology and size distribution of PL-SrO nanoparticles in detail. TEM images of PL-SrO nanoparticles demonstrated spherical morphology, consistent with that of pure SrO Figure 1c. A subtle change in contrast was observed. The PL-SrO nanoparticles displayed a marginally less pronounced edge in comparison to pure SrO,

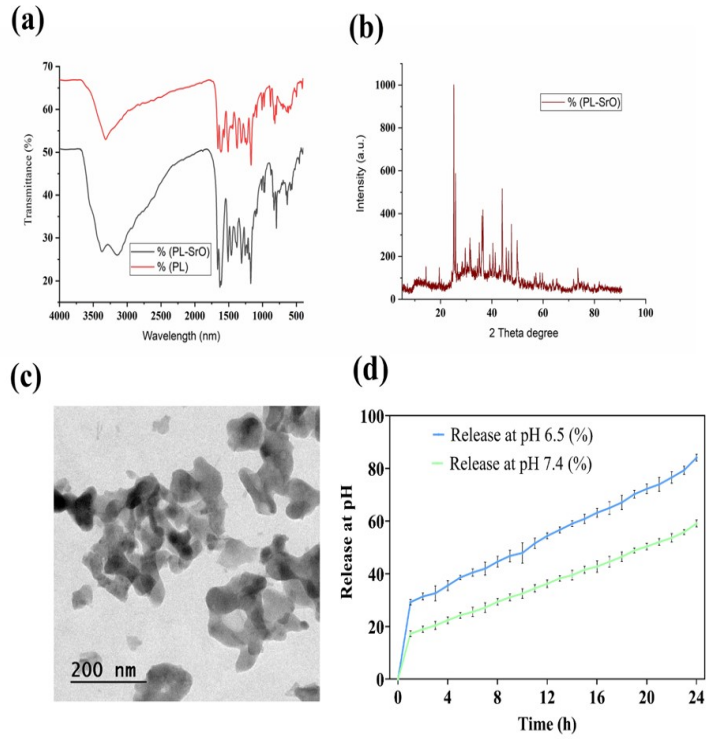

Figure 1: (a) FTIR spectra comparing PL, and PL-SrO highlighting functional group interactions. (b) XRD pattern of PL-SrO, showing its crystalline structure. (c) TEM images illustrating the morphology and size of PL-SRO. (d) PL release profiles from PL-SrO at pH 6.5 and 7.4, showing pH-dependent release

indicating the potential presence of a surface coating or a less defined surface layer. TEM images verified the preservation of the crystalline structure of SrO, with discernible lattice fringes. The average particle size was maintained within the 30-40 nm range, suggesting that the incorporation of PL did not substantially affect the particle size. The PL-SrO nanoparticles exhibited a more uniform particle distribution and reduced agglomeration compared to pure SrO. The TEM results validate the successful synthesis of pelargonidin-loaded SrO nanoparticles exhibiting controlled size and morphology.

3.5. PL- release from PL-SrO

The *in vitro* release kinetics of PL from PL-SrO nanoparticles were examined at pH 7.4 (physiological) and pH 6.5 (simulating the tumor microenvironment) over a 24-hour duration to evaluate the potential of these nanoparticles for controlled drug delivery [39]. The release profile exhibited a biphasic pattern at pH 7.4. A preliminary release of 18% of the encapsulated PL transpired within the initial hour Figure 1d. The rapid release phase is likely due to the release of PL molecules that are adsorbed onto the nanoparticle surface. A sustained release pattern was observed, with a cumulative release of 60% of PL after 24 hours. The sustained release indicates a diffusion-controlled mechanism in which PL molecules are progressively released from the SrO matrix.

At pH 6.5, a notably higher initial burst release of 30% was recorded within the first hour. The improved initial release at acidic pH suggests heightened PL solubility and possible partial degradation of the SrO matrix, leading to accelerated PL release. The cumulative release over 24 hours reached 85% at pH 6.5, indicating a significantly greater release than at pH 7.4. The pH-dependent release behavior highlights the sensitivity of PL-SrO nanoparticles to environmental pH, a trait that is advantageous for targeted drug delivery in acidic tumor microenvironments. The differences in release kinetics observed between the two pH conditions can be attributed to several factors: Increased solubility of PL at lower pH enhances the rate of dissolution and release. Potential partial degradation of the SrO matrix at pH 6.5 may result in increased PL release. Altered surface interactions between PL and SrO at varying pH levels influence the diffusion rate of PL. Our findings demonstrate the capability of PL-SrO nanoparticles for pH-responsive drug delivery. The increased PL release at pH 6.5 indicates that these nanoparticles may be effectively employed for targeted delivery to tumor sites, which generally exhibit an acidic extracellular pH. The controlled release profile at pH 7.4 suggests the capability for prolonged drug release under physiological conditions, thereby reducing systemic side effects.

3.6. Cell culture

Cell proliferation assay

The cell proliferation assay assessed the cytotoxic effects of DOX, PL and PL-SrO nanoparticles on TNBC cells MDA-MB-231 following a 24-h treatment, utilizing concentrations from 0.2 to 8 μg/mL Figure 2a. All tested compounds demonstrated a dose-dependent inhibition of cell proliferation, exhibiting varying levels of potency [39]. DOX, recognized as the standard chemotherapeutic agent, exhibited the highest cytotoxic activity, with an IC_{50} value of 1.5 μg/mL, thereby affirming its established efficacy. PL, a natural compound, exhibited moderate cytotoxicity, with an IC_{50} value of 7.2 μg/mL. This indicates lower potency relative to DOX, yet suggests potential therapeutic applications owing to its natural origin. The PL-SrO nanoparticles demonstrated a markedly increased cytotoxic activity, evidenced by an IC_{50} value of

2.8 μg/mL Figure 2b. The observed reduction in IC_{50}, in comparison to pure PL, underscores the effectiveness of the SrO nanoparticle delivery system in enhancing the cytotoxic effects of PL. The observed enhancement is attributable to several factors: facilitated cellular uptake of PL mediated by SrO nanoparticles, sustained release of PL ensuring prolonged cellular exposure, and potential synergistic cytotoxic effects between PL and SrO. The PL-SrO nanoformulation showed a higher IC_{50} value than DOX, suggesting reduced potency; however, it revealed a significant enhancement in efficacy relative to pure pelargonidin. This indicates that the nanoformulation significantly improves the therapeutic potential of pelargonidin. The increase in cytotoxicity of PL-SrO nanoparticles relative to free pelargonidin indicates the effectiveness of the nano-formulation in enhancing the therapeutic index of pelargonidin. Our finding highlights the potential of PL-SrO nanoparticles as an effective drug delivery system for PL, providing a targeted therapeutic approach for TNBC.

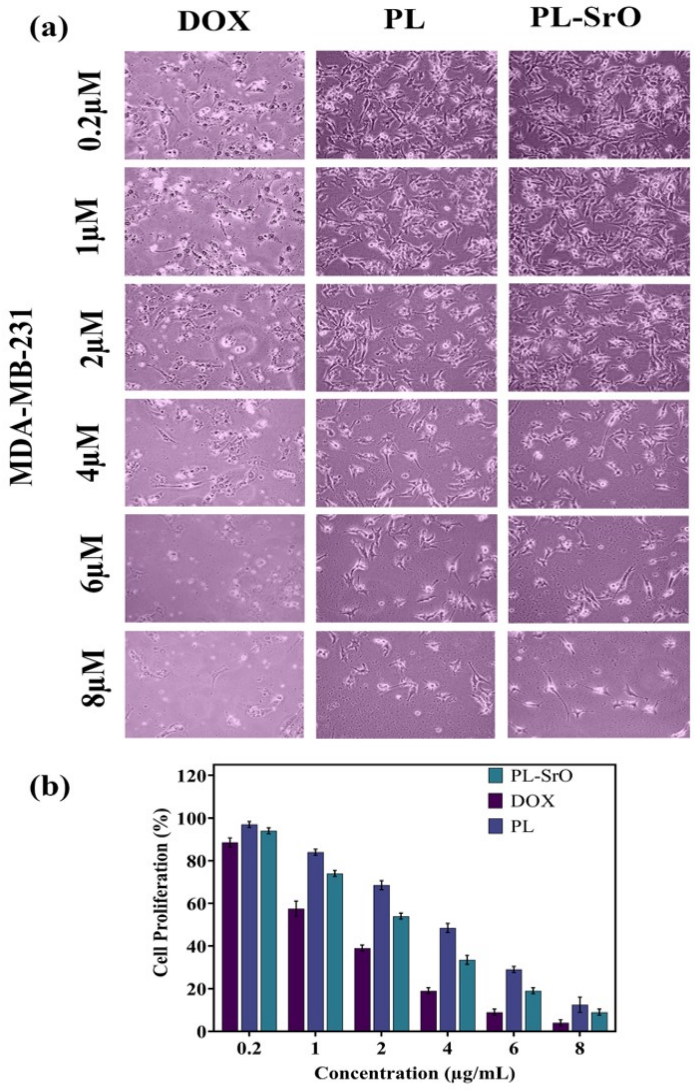

Figure 2: (a) Cell Proliferation assay of MDA-MB-231 after 24 hours of treatment with DOX, PL, and PL-SrO. (b) Percentage cell viability of MDA-MB-231 and MCF-10A cells following 24-hour exposure to DOX, HIS, and HIS-AgNP

Cell compatibility assay

The cell proliferation assay, coupled with morphological observations, was conducted to evaluate the cytotoxic effects and cellular impact of DOX, PL, and PL-SrO nanoparticles on the MCF10A, using concentrations from 0.2 to 8 μg/mL over 24 hours Figure 3a, b. The cell proliferation assay revealed distinct toxicity profiles: DOX significantly reduced cell proliferation to 35% at 8 μg/mL, PL exhibited mild toxicity with 80% proliferation, and PL-SrO nanoparticles demonstrated minimal toxicity, maintaining 90% proliferation at the highest concentration.

Morphological observations corroborated these findings. Untreated cells displayed a typical epithelial cobblestone morphology. DOX-treated cells exhibited significant shrinkage, membrane blebbing, and nuclear fragmentation, indicative of apoptosis, and disrupted monolayer integrity. PL-treated cells showed milder shrinkage and disorganization, while PL-SrO nanoparticle-treated cells maintained their normal epithelial morphology with intact monolayers, showing only a slight reduction in density at the highest concentration. The combined results highlight the stark difference in toxicity profiles. DOX-induced severe cytotoxic effects and significant morphological changes, reflecting its non-selective toxicity. PL exhibited moderate toxicity, with milder morphological alterations. Notably, PL-SrO nanoparticles demonstrated the most favorable safety profile, showing minimal cytotoxicity and maintaining normal cell morphology. Our finding suggests that the

SrO nanoparticles effectively enhance the biocompatibility of PL. The controlled release of pelargonidin, surface modifications of the nanoparticles, and potential protective effects of the SrO matrix likely contribute to the reduced toxicity.

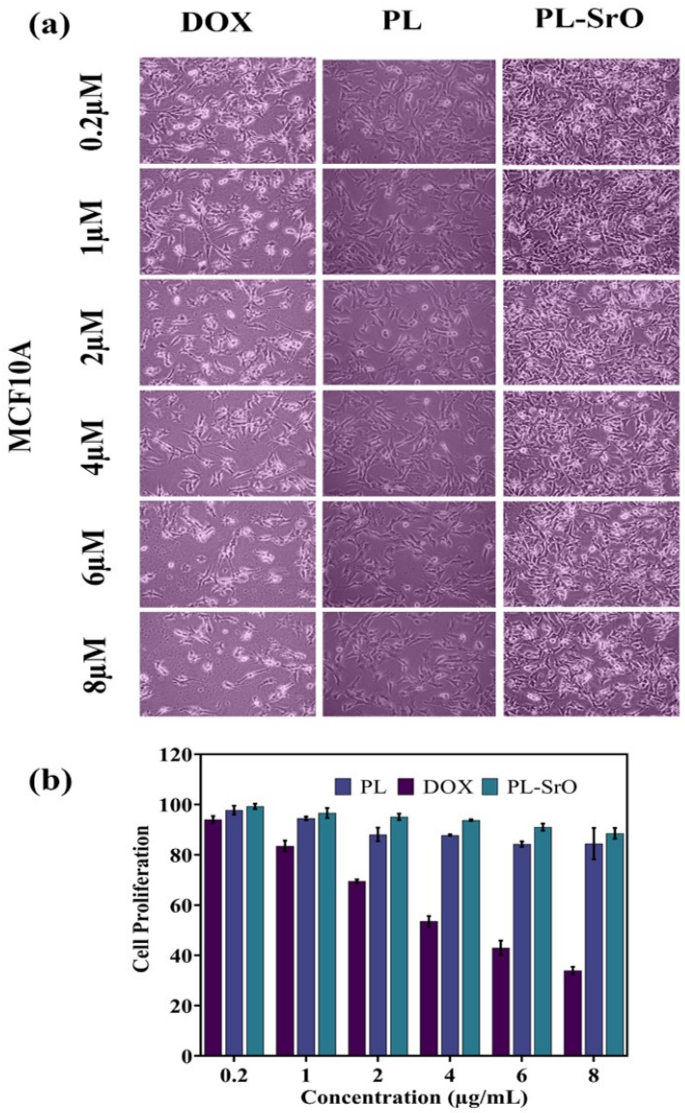

Figure 3: (a) Cell combability assay of MCF-10A cells after 24 hours of treatment with DOX, PL, and PL-SrO. (b) Cell Viability (24h): Percentage cell viability of MCF-10A cells following 24-hour exposure to DOX, PL, and PL-SrO

Cellular uptake assay

The cellular uptake assay, an essential method for assessing the effectiveness of drug delivery systems, was conducted utilizing FITC-labeled DOX, PL, and PL-SrO nanoparticles Figure 4a. The internalization dynamics of these compounds in TNBC cells, treated at their respective IC_{50} values, and in MCF10A cells treated at a fixed concentration of 8 μg/mL, were examined over a time course of 0, 2, and 4 hours Figure 4b. Analyzing the differing uptake patterns of cancerous versus normal cells is essential for evaluating the selectivity and therapeutic efficacy of the PL-SrO nanoformulation. At the initial time point (0 hours), both cell lines displayed minimal fluorescence, indicating a lack of significant compound internalization before treatment. After two hours, distinct uptake patterns were observed. In MDA-MB-231 cells, DOX demonstrated pronounced, diffuse cytoplasmic fluorescence, reflecting rapid and effective internalization, in alignment with its known mechanism of action. Cells treated with PL exhibited moderate fluorescence, indicating a reduced uptake rate, predominantly localized in the cytoplasm. PL-SrO-treated cells exhibited punctate fluorescence, indicative of nanoparticle internalization through endocytic pathways and subsequent intracellular distribution. This observation indicates that SrO nanoparticles enhanced the uptake of PL into cancer cells via a mechanism distinct from simple diffusion. At the 4-hour mark, the fluorescence intensity in MDA-MB-231 cells exhibited an increase for all compounds. Cells treated with DOX exhibited a sustained increase in diffuse cytoplasmic fluorescence. Cells treated with PL demonstrated a significant increase in cytoplasmic fluorescence, suggesting enhanced uptake. PL-SrO-treated cells exhibited a significant increase in punctate fluorescence, indicating the time-dependent accumulation of nanoparticles within the cells. In contrast, MCF10A cells demonstrated markedly reduced uptake levels.

After 2 hours, DOX-treated MCF10A cells exhibited moderate diffuse fluorescence, though less intense than that observed in MDA-MB-231, indicating a reduced uptake rate in normal cells. Cells treated with PL exhibited weak cytoplasmic fluorescence, suggesting limited internalization. Cells treated with PL-SrO displayed minimal punctate fluorescence, indicating a restricted uptake of nanoparticles by normal

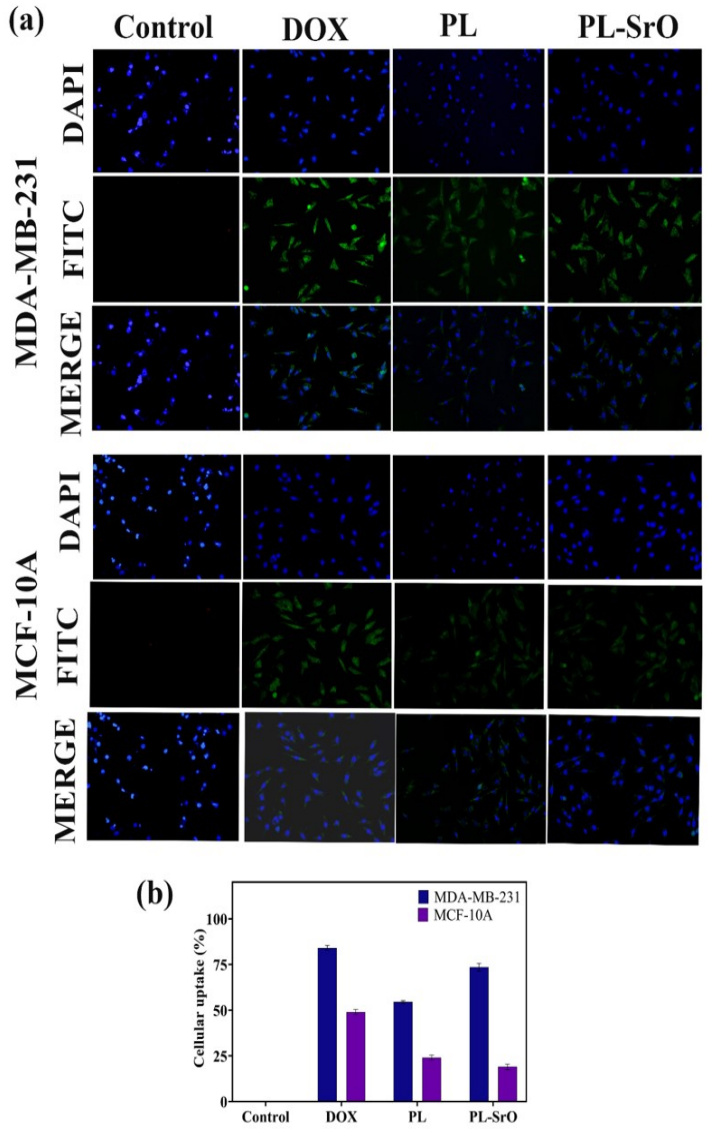

Figure 4: (a) Cellular internalization of FITC-labeled DOX, PL, and PL-SrO in MDA-MB-231 MCF-10A cells after 4 hours of treatment. b) Graphical representation of DOX, PL, and PL-SrO internalization in MDA-MB-231 and MCF-10A cells at 4 hours

cells. After 4 hours, DOX fluorescence in MCF10A cells increased, yet it remained lower compared to MDA-MB-231 cells. PL and PL-SrO uptake exhibited minor increases, yet remained significantly lower compared to cancer cells. The quantitative analysis of cellular uptake supported the morphological observations. In MDA-MB-231 cells, the uptake of DOX was 85% at 4 hours, while PL uptake was 55% and PL-SrO uptake was 75%. In MCF10A cells, the uptake was significantly lower, with DOX at 50%, PL at 25%, and PL-SrO at 20%. The quantitative data underscore the differing uptake patterns, illustrating the increased internalization of PL-SrO nanoparticles in cancer cells relative to normal cells. The increased absorption of PL-SrO in MDA-MB-231 cells, alongside its limited absorption in MCF10A cells, indicates that SrO nanoparticles may enable targeted delivery of pelargonidin to cancer cells, possibly through receptor-mediated endocytosis or other specific internalization pathways. The selective uptake reduces the likelihood of systemic toxicity, which is a crucial consideration in cancer treatment.

Colony formation assay

The assessment of long-term cytotoxic effects was conducted using the colony formation assay on TNBC cells, employing DOX, PL, and PL-SrO nanoparticles at their respective IC_{50} values after a 24-hour initial exposure Figure 5a. Microscopic analysis of untreated cells demonstrated the presence of numerous large, densely populated colonies, suggesting a strong clonogenic capacity. DOX-treated cells demonstrated a significant reduction in colony formation, characterized by small, sparse, and fragmented colonies, which aligns with its strong cytotoxic mechanism [32, 47]. PL-treated cells exhibited a moderate decrease in colony size and density, indicating a significant,Though less pronounced, inhibitory effect. PL-SrO-treated cells exhibited a significant decrease in colony formation, resulting in minimal and poorly defined colonies, which suggests improved long-term cytotoxic efficacy. Quantitative analysis supported these findings Figure 5b. Untreated control exhibited 100% colony formation; DOX resulted in 15% ($p < 0.001$); PL showed 40% ($p < 0.01$); and PL-SrO demonstrated 10% ($p < 0.001$). The notable decrease observed with DOX corresponds with its recognized cytotoxic mechanism. PL exhibited a moderate inhibitory effect, whereas PL-SrO nanoparticles showed the most significant reduction, matching and in some instances slightly exceeding DOX. This effect is likely due to the sustained release of PL and improved intracellular delivery enabled by the nanoparticle

matrix. The significant p-values for DOX and PL-SrO highlight the statistical strength of these findings. The prolonged cytotoxic effect of PL-SrO underscores its potential as an effective therapeutic agent for TNBC, indicating a promising approach for preventing tumor recurrence and metastasis.

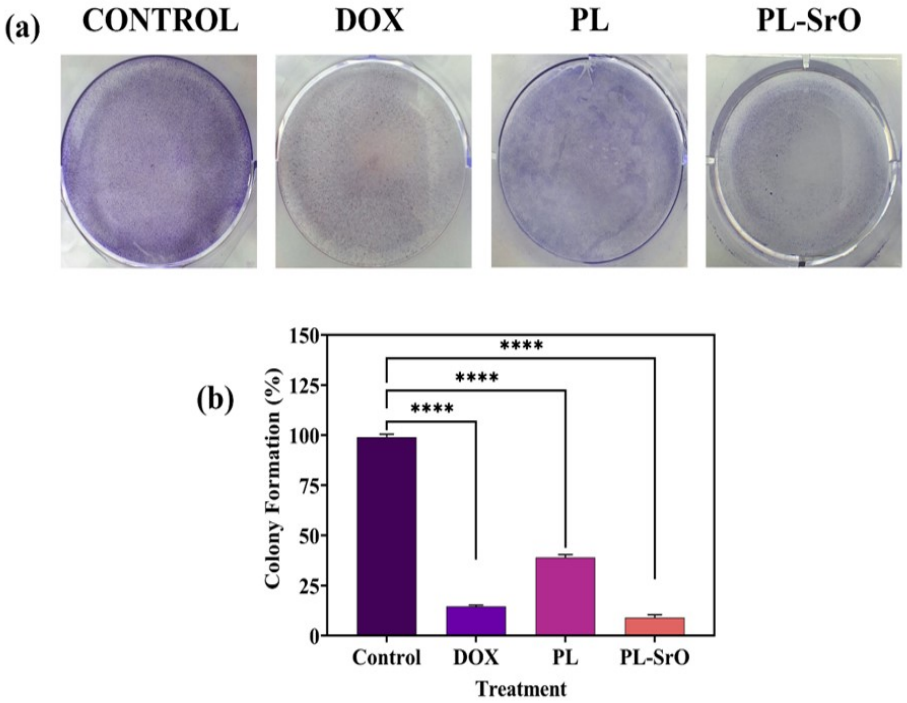

Figure 5: (a) Colony formation assay of in MDA-MB-231 after 24-hour treatment with DOX, PL, and PL-SrO (b) Graphical representation of colony formation in MDA-MB-231 after 24-hour treatment with DOX, PL, and PL-SrO

Migration assay

The migration assay assessed the effects of DOX, PL and PL-SrO nanoparticles on the motility of TNBC cells Figure 6a. Microscopic observation of untreated cells at 24 hours revealed significant migration characterized by spindle-like morphology, whereas DOX-treated cells demonstrated a notable decrease in migration, presenting rounded, less elongated shapes, while overall cell count remained comparable. PL-treated cells exhibited a marked reduction in cell elongation, resulting in fewer and less elongated cells. In contrast, PL-SrO-treated cells demonstrated the most pronounced reduction, characterized by minimal, rounded cells; however, the overall cell count remained comparable. Quantitative analysis validated these findings Figure 6b: control exhibited 100% migration; DOX resulted in 30% ($p < 0.001$); PL showed 60% ($p < 0.01$); and PL-SrO demonstrated 15% ($p < 0.001$) DOX markedly decreased migration, indicating its strong cytotoxic effect, whereas PL exhibited a moderate inhibitory effect. PL-SrO nanoparticles demonstrated a significant reduction, matching or exceeding that of DOX, likely attributable to the sustained release of pelargonidin and improved intracellular delivery. The cell count in each treatment group did not significantly differ, suggesting that the changes in migration were not attributable to overall cell death, but rather to a direct effect on cell motility. Our findings indicate PL-SrO potential as an effective therapeutic agent for inhibiting the TNBC metastasis.

Invasion assay

The invasion assay employed a Matrigel-coated trans well system to evaluate the inhibitory effects of DOX, PL, and PL-SrO nanoparticles on the invasive capacity of TNBC cells Figure 7a.

Microscopic observation of untreated control cells at 24 hours demonstrated significant invasion, with many cells penetrating the Matrigel and adhering to the membrane's underside, exhibiting a morphology characteristic of invasive behavior. Cells treated with DOX exhibited a significant decrease in invasion, as evidenced by a reduced number of cells on the underside of the membrane, while the total cell count remained comparable.

PL-treated cells exhibited a significant decrease in invasion relative to the control, as evidenced by a lower number of cells migrating through the Matrigel while maintaining a comparable cell count to the control group. PL-SrO-treated cells demonstrated the most substantial reduction, with few invasive cells detected, and a comparable cell count relative to the control group. Quantitative analysis validated these findings Figure 7b): control exhibited 100% invasion; DOX resulted in 20% ($p < 0.001$); PL demonstrated 50% ($p < 0.01$); and PL-SrO showed 10% ($p < 0.001$) Figure 7b. DOX markedly reduced invasion, indicating its strong cytotoxic and anti-invasive properties, whereas PL exhibited a moderate inhibitory effect. PL-SrO nanoparticles demonstrated a significant reduction, matching or exceeding that of DOX, likely attributable to sustained PL release and improved intracellular delivery. The cell count in each treatment group did not significantly differ, suggesting that the changes in invasion were not attributable to overall cell death, but rather to a direct effect on the cells' capacity to penetrate the Matrigel barrier. Our findings indicate that PL-SrO serves as a highly effective therapeutic agent for the inhibition of tumor invasion and metastasis.

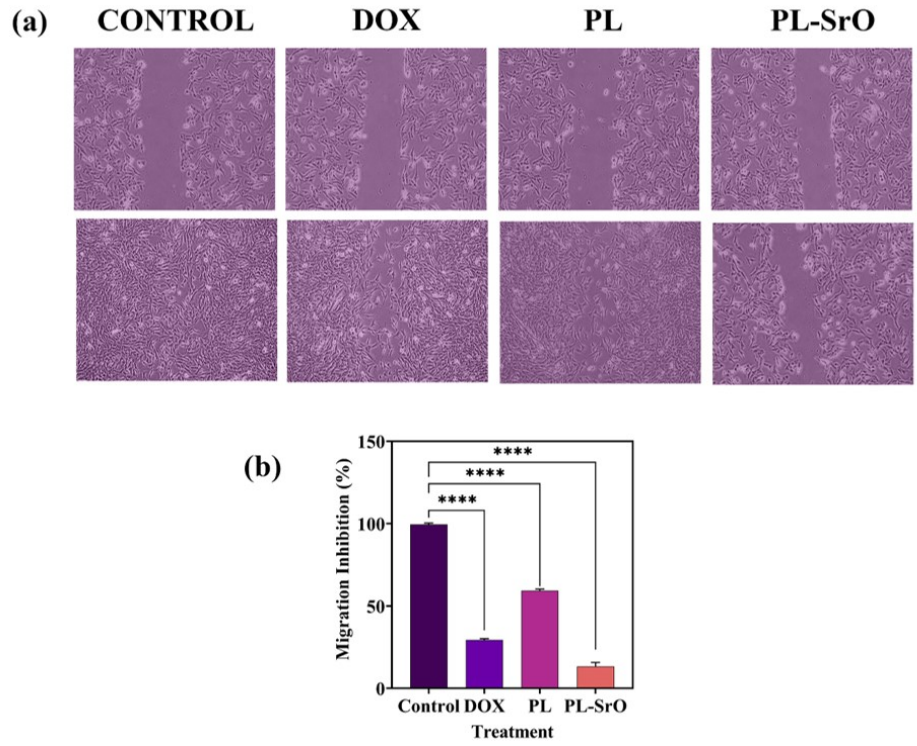

Figure 6: (a) Cell migration assay of MDA-MB-231 after 24-hour treatment with DOX, PL, and PL-SrO (b) Graphical representation of cell migration in MDA-MB-231 and MDA-MB-468 cells after 24-hour treatment with DOX, PL, and PL-SrO

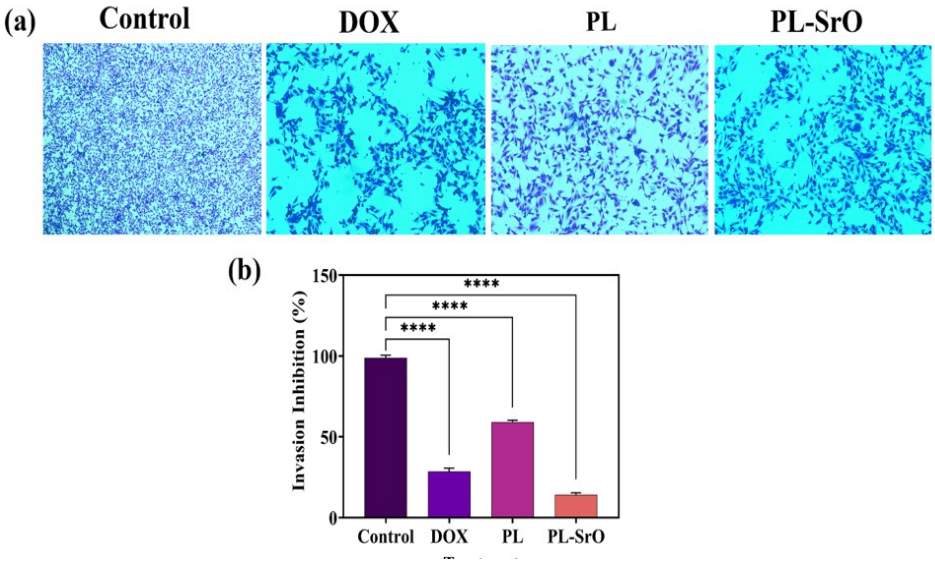

Figure 7: Cell Invasion assay of MDA-MB-231 after 24-hour treatment with DOX, PL, and PL-SrO (b) Graphical representation of cell migration in MDA-MB-231 and MDA-MB-468 cells after 24-hour treatment with DOX, PL, and PL-SrO

Apoptotic staining assay

The apoptotic staining assay was performed to assess apoptosis induction in TNBC cells after a 24-hour IC_{50} treatment with DOX, PL, and PL-SrO nanoparticles Figure 8. Microscopic examination of untreated control cells demonstrated a predominance of bright green cells, signifying viable cells with intact DNA. DOX-treated cells exhibited a notable shift, characterized by a substantial presence of orange-red cells, indicative of late apoptosis or necrosis, alongside some bright orange cells, which represent early apoptosis. PL-treated cells exhibited a moderate increase in orange cells, including some bright orange, indicative of both early and late apoptosis; however, a substantial number of viable green cells persisted. PL-SrO-treated cells exhibited a significant shift, characterized by a high prevalence of orange-red and bright orange cells, which in some instances equaled or exceeded the effects of DOX, suggesting a strong induction of apoptosis. DOX significantly induced apoptosis, consistent with its established mechanism, whereas PL exhibited a moderate apoptotic effect. PL-SrO nanoparticles demonstrated significant apoptotic induction, comparable to and in certain instances exceeding that of DOX, likely attributable to prolonged pelargonidin release and improved intracellular delivery. Our findings indicate that PL-SrO directly correlates with the degree of cellular

damage and apoptosis in TNBC cells.

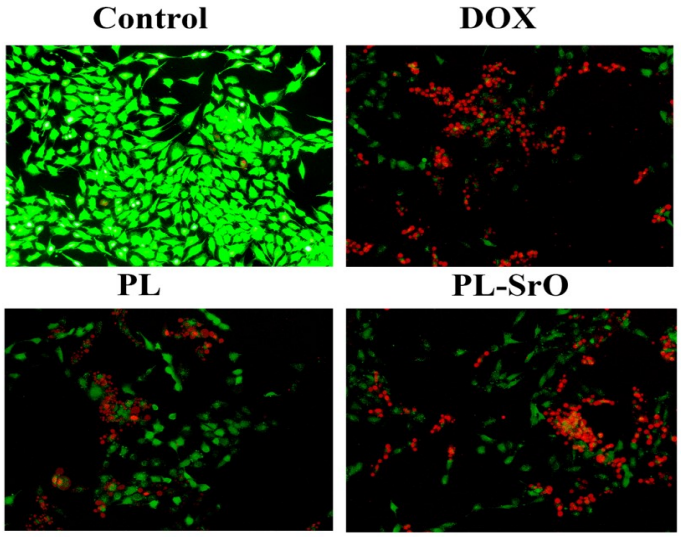

Figure 8: Apoptotic staining assay of MDA-MB-231 after 24-hour treatment with DOX, PL, and PL-SrO

Assessment of MMP level

The MMP estimation utilized RhO to evaluate the effects of DOX, PL, and PL-SrO nanoparticles on TNBC cells Figure 9a. This assay is essential for assessing mitochondrial integrity, given that MMP disruption signifies apoptosis and cellular dysfunction. Microscopic examination of untreated control cells demonstrated pronounced green fluorescence, signifying elevated mitochondrial membrane potential and healthy mitochondria. Cells treated with DOX exhibited a marked reduction in green fluorescence, indicating a substantial loss of mitochondrial membrane potential and mitochondrial dysfunction. Cells treated with PL demonstrated a moderate decrease in green fluorescence, suggesting a partial reduction in MMP. Cells treated with PL-SrO exhibited a significant reduction in green fluorescence, comparable to and in some instances exceeding that of DOX, suggesting considerable mitochondrial impairment. Quantitative analysis validated these findings Figure 9b. Control exhibited a 100% MMP level; DOX showed a 20% MMP level ($p < 0.001$); PL demonstrated a 60% MMP level ($p < 0.01$); and PL-SrO indicated a 10% MMP level ($p < 0.001$). DOX markedly impaired MMP, indicating its established mitochondrial toxicity, whereas PL exhibited a moderate decrease. PL-SrO nanoparticles demonstrated the most pronounced disruption of MMP, matching or exceeding the effects of DOX, likely attributable to sustained PL release and improved intracellular delivery. The overall cell morphology and cell count in each treatment group did not significantly differ, suggesting that the changes in MMP were not attributable to cell death, but rather to a direct impact on mitochondrial function. Our findings indicate that PL-SrO has the potential to be a potent inducer of mitochondrial dysfunction in TNBC.

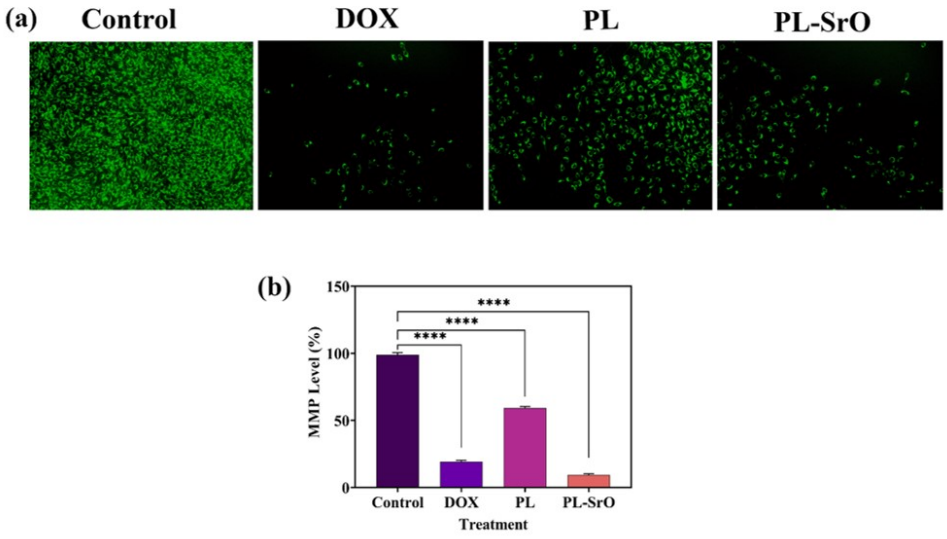

Figure 9: (a) MMP assay of MDA-MB-231 and MDA-MB-468 cells after 24-hour treatment with DOX, PL, and PL-SrO; (b) Graphical representation of MMP activity in MDA-MB-231 and MDA-MB-468 cells after 24-hour treatment with DOX, PL, and PL-SrO

Intercellular ROS production

The ROS production assay was performed to evaluate the effects of DOX, PL, and PL-SrO nanoparticles on TNBC cells Figure 10a. This assay is important as ROS, although necessary for cellular signaling at low concentrations, can cause considerable cellular damage and apoptosis when present in excess, thereby representing a critical target in cancer therapy [48]. Microscopic examination of untreated control cells demonstrated minimal green fluorescence, suggesting low basal levels of ROS. Cells treated with DOX exhibited a marked increase in green fluorescence, indicating a substantial rise in ROS production. Cells treated with PL demonstrated a moderate increase in green fluorescence, suggesting a partial elevation of ROS.

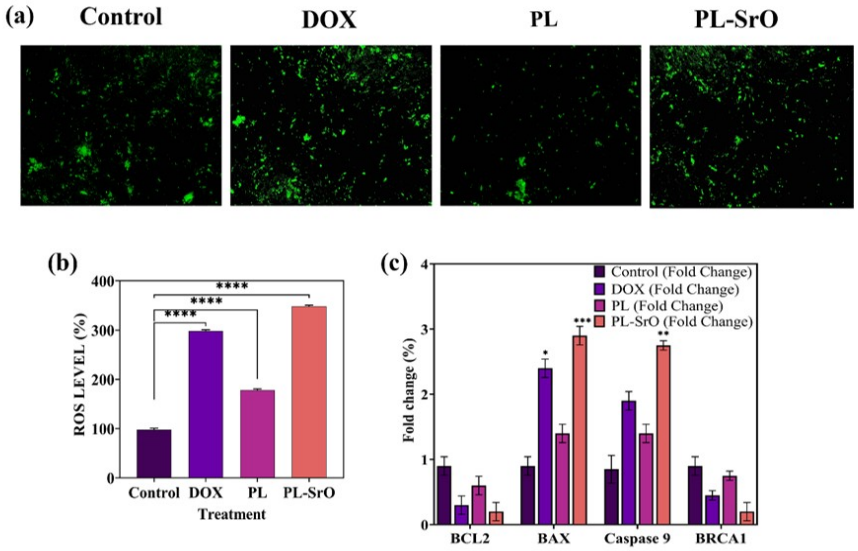

Figure 10: (a) Evaluation of intracellular ROS levels in MDA-MB-231 and MDA-MB-468 cells after 24-hour treatment with DOX, PL, and PL-SrO. (b) Graphical representation of ROS levels in MDA-MB-231 cells after 24-hour treatment with DOX, PL, and PL-SrO (c) Apoptosis Gene Expression (24h): Apoptotic gene expression analysis in MDA-MB-231 cells after 24-hour treatment with DOX, PL, and PL-SrO

PL-SrO-treated cells exhibited the most significant increase in green fluorescence, reflecting and, in some instances, exceeding that of DOX, which indicates a marked generation of ROS. Quantitative analysis validated these findings: control exhibited a 100% basal ROS level; DOX demonstrated a 300% ROS level ($p < 0.001$); PL showed a 180% ROS level ($p < 0.01$); and PL-SrO indicated a 350% ROS level ($p < 0.001$) Figure 10b. DOX markedly increased ROS production, consistent with its established oxidative stress mechanism, whereas PL exhibited a moderate rise. PL-SrO nanoparticles demonstrated the highest levels of ROS generation, matching or exceeding those of DOX, likely attributable to prolonged pelargonidin release and improved intracellular delivery. The overall cell morphology and cell count in each treatment group did not significantly differ, suggesting that the changes in ROS levels were not attributable to cell death, but rather to a direct effect on intracellular ROS production. Our findings indicate that PL-SrO has significant potential as an inducer of ROS generation in TNBC.

3.7. Gene expression analysis

Quantitative RT-PCR was utilized to examine the effects of DOX, PL, and PL-SrO nanoparticles on the expression of critical apoptosis and DNA repair genes-BCL2, BAX, Caspase 9, and BRCA1—in TNBC cells Figure 10c. This analysis sought to clarify the molecular mechanisms responsible for the observed cytotoxic effects. Untreated control cells functioned as a reference point (fold change = 1). DOX treatment led to a notable downregulation of BCL2 (fold change 0.4, $p < 0.001$) and BRCA1 (fold change 0.5, $p < 0.001$), alongside a significant upregulation of BAX (fold change 2.5, $p < 0.001$) and Caspase 9 (fold change 2.0, $p < 0.001$), aligning with its known mechanisms of inducing apoptosis and DNA damage. PL treatment resulted in a statistically significant downregulation of BCL2 (fold change 0.7, $p < 0.01$) and BRCA1 (fold change 0.8, $p < 0.05$), alongside a moderate upregulation of BAX (fold change 1.5, $p < 0.05$) and Caspase 9 (fold change 1.3, $p < 0.05$). PL-SrO nanoparticles induced significant alterations in gene expression, characterized by a notable downregulation of BCL2 (fold change 0.3, $p < 0.001$) and BRCA1 (fold change 0.3, $p < 0.001$), alongside a substantial upregulation of BAX (fold change 3.0, $p < 0.001$) and Caspase 9 (fold change 2.8, $p < 0.001$), in certain cases surpassing the effects observed with DOX.

The observed alterations in gene expression elucidate the underlying mechanisms of action. BCL2, an anti-apoptotic protein, and BAX, a pro-apoptotic protein, play crucial roles in the mitochondrial pathway of apoptosis [49–51]. The notable downregulation of BCL2 and upregulation of BAX by PL-SrO, resulting in an elevated BAX/BCL2 ratio, indicates the induction of mitochondrial-mediated apoptosis. Caspase 9, an initiator caspase in the intrinsic apoptotic pathway [52], exhibited significant upregulation due to PL-SrO and DOX, suggesting the activation of the apoptotic cascade. The activation is directly correlated with the observed changes in BCL2 and BAX, as the mitochondrial pathway initiates Caspase 9 activation. BRCA1, a protein involved in DNA repair [53, 54] was significantly downregulated by PL-SrO and DOX, indicating a reduction in the cell's capacity to repair DNA damage. This disruption, along with the induction of apoptosis, contributes to the overall cytotoxic effect. The improved gene expression modulation associated with PL-SrO nanoparticles is likely due to the sustained release of pelargonidin and enhanced intracellular delivery enabled by the nanoparticle matrix, thereby increasing bioavailability and efficacy. The significant p-values for PL-SrO and DOX highlight the statistical strength of these findings.

Our findings indicate that PL-SrO nanoparticles significantly influence critical apoptotic and DNA repair genes, showing greater therapeutic potential than free PL and similar efficacy to DOX. The correlated gene expression changes elucidate the mechanistic basis of the observed cytotoxic effects, underscoring the potential of PL-SrO nanoparticles as an effective targeted drug delivery system for TNBC.

4. Conclusion

PL-SrO nanoparticles were synthesized using a co-precipitation method, resulting in high entrapment efficiency and controlled release kinetics. Characterization through FTIR, XRD, and TEM validated the formation of crystalline SrO nanoparticles exhibiting uniform PL distribution. *In vitro* release studies demonstrated pH-responsive drug release, showing increased pelargonidin release in acidic conditions that mimic the tumor microenvironment. Biological assays on TNBC cells indicated that PL-SrO nanoparticles displayed notable cytotoxic effects, exceeding those of free PL and, in certain cases, matching or surpassing the efficacy of DOX. PL-SrO nanoparticles exhibited increased cellular uptake in MDA-MB-231 cells relative to MCF10A normal cells, suggesting selectivity. The nanoparticles significantly reduced colony formation, migration, and invasion, underscoring their potential as anti-metastatic agents. Additionally, PL-SrO significantly induced apoptosis disrupted MMP, and increased ROS production. Gene expression analysis indicated that PL-SrO nanoparticles significantly influenced key apoptosis and DNA repair genes, such as BCL2, BAX, Caspase 9, and BRCA1, highlighting a strong induction of mitochondrial-mediated apoptosis and interference with DNA repair processes. The molecular insights highlight the therapeutic potential of PL-SrO nanoparticles as a targeted drug delivery system for TNBC. Future in *vivo* studies are necessary to validate these findings and evaluate the therapeutic efficacy of PL-SrO nanoparticles in preclinical models.

Article Information

Author contributions: P.Z. - Conceptualization methodology; C.W. - Validation, Formal analysis, Investigation; M.Q. - Validation, Formal analysis, Investigation; Q.H. - Resources, Data curation; W.L. - Writing—original draft preparation, Writing—review and editing, Visualization, Supervision, Project administration, Funding acquisition; Y.Z. - Writing—original draft preparation, Writing—review and editing, Visualization, Supervision, Project administration, Funding acquisition.

Data availability: The datasets used and/or analyzed during the current study are available from the corresponding author Ying Zhang on reasonable request via e-mail yz1660590@gmail.com.

Competing Interests: Authors have declared that no competing interests exist.

Disclaimer (Artificial Intelligence): The author(s) hereby declare that NO generative AI technologies such as Large Language Models (ChatGPT, COPILOT, etc.), and text-to-image generators have been used during writing or editing of manuscripts.

References

[1] *Breast Cancer*. World Health Organization. URL https://www.who.int/news-room/fact-sheets/detail/breast-cancer.

[2] H. Liang, G. Yin, D. Feng, H. Chen, X. Liu, and J. Li. Research Trends on Nanomaterials in Triple Negative Breast Cancer (TNBC): A Bibliometric Analysis from 2010 to 2024. *Drug Delivery and Translational Research*, 16:1650–1665, 2024. URL https://doi.org/10.1007/s13346-024-01704-9.

[3] F. M. Howard and O. I. Olopade. Epidemiology of Triple-Negative Breast Cancer. *The Cancer Journal*, 27(1):8–16, 2021. URL https://doi.org/10.1097/ppo.0000000000000500.

[4] N. Roy and A. Mathew. Triple Negative Breast Cancer in India: What Is the Real Incidence? *Indian Journal of Medical and Paediatric Oncology*, 44(4):442–444, 2022. URL https://doi.org/10.1055/s-0042-1742612.

[5] S. Sarkar. Triple Negative Breast Cancer Prevalence in Indian Patients over a Decade: A Systematic Review. *International Journal of Clinical Biostatistics and Biometrics*, 8(1):1–9, 2022. doi:10.23937/2469-5831/1510045.

[6] Y. Khan, S. Rizvi, A. Raza, A. Khan, S. Hussain, N. U. Khan, S. O. Alshammari, Q. A. Alshammari, Abdulkarim Alshammari, and Doha El-Sayed Ellakwa. Tailored Therapies for Triple-Negative Breast Cancer: Current Landscape and Future Perceptions. *Naunyn-Schmiedeberg s Archives of Pharmacology*, 398:9425–9450, 2025. URL https://doi.org/10.1007/s00210-025-03896-4.

[7] A. C. Garrido-Castro, N. U. Lin, and K. Polyak. Insights into Molecular Classifications of Triple-Negative Breast Cancer: Improving Patient Selection for Treatment. *Cancer Discovery*, 9(2):176–198, 2019. URL https://doi.org/10.1158/2159-8290.cd-18-1177.

[8] M. Pont, M. Marqués, and A. Sorolla. Latest Therapeutical Approaches for Triple-Negative Breast Cancer: From Preclinical to Clinical Research. *International Journal of Molecular Sciences*, 25(24):13518, 2024. URL https://doi.org/10.3390/ijms25241351.

[9] P. Malla, Y.M. Wang, and C.H. Su. New Horizons for the Therapeutic Application of Nanozymes in Cancer Treatment. *Journal of Nanobiotechnology*, 23(1), 2025. URL https://doi.org/10.1186/s12951-025-03185-5.

[10] Nanotechnology Cancer Therapy and Treatment - NCI. [Accessed March 10, 2025], 2017. URL https://www.cancer.gov/nano/cancer-nanotechnology/treatment.

[11] R. D. Al Bostami, W. H. Abuwatfa, and G. A. Husseini. Recent Advances in Nanoparticle-Based Co-Delivery Systems for Cancer Therapy. *Nanomaterials*, 12(15):1–26, 2022. URL https://doi.org/10.3390/nano12152672.

[12] L. Yue, Y. Li, Y. Luo, A. A. Alarfaj, and Y. Shi. Pelargonidin Inhibits Cell Growth and Promotes Oxidative Stress-Mediated Apoptosis in Lung Cancer A549 Cells. *Biotechnology and Applied Biochemistry*, 71(5), 2024. https://doi.org/10.1002/bab.2621.

[13] C. Felgines, O. Texier, C. Besson, B. Lyan, J.sL. Lamaison, and A. Scalbert. Strawberry Pelargonidin Glycosides Are Excreted in Urine as Intact Glycosides and Glucuronidated Pelargonidin Derivatives in Rats. *British Journal of Nutrition*, 98(6):1126–1131, 2007. URL https://doi.org/10.1017/s0007114507764772.

[14] K. Alzbeta, E. Anzenbacherova, P. Pavek, A.A. Soshilov, M.S. Denison, P. Anzenbacher, and Z Dvorak. Pelargonidin Activates the AhR and Induces CYP1A1 in Primary Human Hepatocytes and Human Cancer Cell Lines HepG2 and LS174T. *Toxicology Letters*, 218(3):253–259, 2013. URL https://doi.org/10.1016/j.toxlet.2013.01.020.

[15] A. Kamenickova, E. Anzenbacherova, P. Pavek, A. A. Soshilov, M. S. Denison, P. Anzenbacher, and Z Dvorak. Pelargonidin Activates the AhR and Induces CYP1A1 in Primary Human Hepatocytes and Human Cancer Cell Lines HepG2 and LS174T. *Toxicology Letters*, 218(3):253–259, March 2013. URL https://doi.org/10.1016/j.toxlet.2013.01.020.

[16] W. Li, M. Gu, P. Gong, J. Wang, Y. Hu, Y. Hu, X. Tan, J. Wei, and H. Yang. Glycosides Changed the Stability and Antioxidant Activity of Pelargonidin. *LWT*, 147:111581–111581, 2021. URL https://doi.org/10.1016/j.lwt.2021.111581.

[17] Y. Noda, T. Kaneyuki, A. Mori, and L. Packer. Antioxidant Activities of Pomegranate Fruit Extract and Its Anthocyanidins: Delphinidin, Cyanidin, and Pelargonidin. *Journal of Agricultural and Food Chemistry*, 50(1):166–171, 2002. URL https://doi.org/10.1021/jf0108765.

[18] I.-C. Lee and J.-S. Bae. Suppressive Effects of Pelargonidin on PolyPhosphate-Mediated Vascular Inflammatory Responses. *Archives of Pharmacal Research*, 40(2):258–267, 2016. URL https://doi.org/10.1007/s12272-016-0856-z.

[19] A. R. Nunes, E. C. Costa, G. Alves, and L. R. Silva. Nanoformulations for the Delivery of Dietary Anthocyanins for the Prevention and Treatment of Diabetes Mellitus and Its Complications. *Pharmaceuticals*, 16(5):736, 2023. URL https://doi.org/10.3390/ph16050736.

[20] Asmita Samadder, Debojyoti Tarafdar, S. Abraham, K. Ghosh, and Anisur Khuda-Bukhsh. Nano-Pelargonidin Protects Hyperglycemic-Induced L6 Cells against Mitochondrial Dysfunction. *Planta Medica*, 83(05):468–475, 2017. URL https://doi.org/10.1055/s-0043-100017.

[21] M. Rezaul, N. Karim, Y. Xu, J. Xie, and W. Chen. Improving the Physicochemical Stability and Functionality of Nanoliposome Using Green Polymer for the Delivery of Pelargonidin-3-O-Glucoside. *Food Chemistry*, 337:127654, 2020. URL https://doi.org/10.1016/j.foodchem.2020.127654.

[22] H. Teng, Y. Zheng, H. Cao, Q. Huang, J. Xiao, and L. Chen. Enhancement of Bioavailability and Bioactivity of Diet-Derived Flavonoids by Application of Nanotechnology: A Review. *Critical Reviews in Food Science and Nutrition*, 63(3):1–16, 2021. URL https://doi.org/10.1080/10408398.2021.1947772.

[23] A. Bakhtiar and E. H. Chowdhury. PH-Responsive Strontium Nanoparticles for Targeted Gene Therapy against Mammary Carcinoma Cells. *Asian Journal of Pharmaceutical Sciences*, 16(2):236–252, 2021. URL https://doi.org/10.1016/j.ajps.2020.11.002.

[24] H. Wang, T. Lakshmipriya, Y. Chen, and S. C. B. Gopinath. Squamous Cell Carcinoma Biomarker Sensing on a Strontium Oxide-Modified Interdigitated Electrode Surface for the Diagnosis of Cervical Cancer. *BioMed Research International*, 2019(1):1–7, 2019. URL https://doi.org/10.1155/2019/2807123.

[25] P. Anbu, B. Gopinath, M.N. Salimi, I. Letchumanan, and S. Subramaniam. Green Synthesized Strontium Oxide Nanoparticles by Elodea Canadensis Extract and Their Antibacterial Activity. *Journal of nanostructure in chemistry*, 12(3):365–373, 2021. URL https://doi.org/10.1007/s40097-021-00420-x.

[26] S. Lanjar, A. R. Solangi, N. Batool, N. H. Khand, M. Kamboh, A. Malah, J. A. Buledi, and M. M. Khan. Strategic Electrochemical Oxidation of Vinblastin Sulfate (an Anticancer Drug) Via PVP-Functionalized Strontium Oxide Nanoparticles. *RSC Advances*, 14(43): 31387–31397, 2024. URL https://doi.org/10.1039/d4ra05493h.

[27] X. Wei, X. Zhang, Z. Yang, L. Li, and H. Sui. Osteoinductive Potential and Antibacterial Characteristics of Collagen Coated Iron Oxide Nanosphere Containing Strontium and Hydroxyapatite in Long Term Bone Fractures. *Arabian Journal of Chemistry*, 14(3), 2021. URL https://doi.org/10.1016/j.arabjc.2020.102984.

[28] Y. Chen, Z. Zheng, R. Zhou, H. Zhang, C. Chen, Z. Xiong, K. Liu, and X. Wang. Developing a Strontium-Releasing Graphene Oxide-/Collagen-Based Organic–Inorganic Nanobiocomposite for Large Bone Defect Regeneration via MAPK Signaling Pathway. *ACS Applied Materials & Interfaces*, 11(17):15986–15997, 2019. URL https://doi.org/10.1021/acsami.8b22606.

[29] J. Ahmad, R. Wahab, M. A. Siddiqui, N. Quaiser Saquib, Ahmad, and A. A. Al-Khedhairy. Strontium-Doped Nickel Oxide Nanoparticles: Synthesis, Characterization, and Cytotoxicity Study in Human Lung Cancer A549 Cells. *Biological Trace Element Research*, 200(4):1598–1607, 2021. URL https://doi.org/10.1007/s12011-021-02780-5.

[30] S. Mukherjee and M. Mishra. Application of Strontium-Based Nanoparticles in Medicine and Environmental Sciences. *Nanotechnology for environmental engineering*, 6(2), 2021. URL https://doi.org/10.1007/s41204-021-00115-2.

[31] S. Wang, . Du Liu Qian Sun, Zhu, and W.-Y. PH-Sensitive Strontium Carbonate Nanoparticles as New Anticancer Vehicles for Controlled Etoposide Release. *International Journal of Nanomedicine*, 5781, 2012. URL https://doi.org/10.2147/ijn.s34773.

[32] O. Tacar, P. Sriamornsak, and C. R. Dass. Doxorubicin: An Update on Anticancer Molecular Action, Toxicity and Novel Drug Delivery Systems. *Journal of Pharmacy and Pharmacology*, 65(2):157–170, 2012. URL https://doi.org/10.1111/j.2042-7158.2012.01567.x.

[33] H. S. Al-malky, S. E. Al Harthi, and A.-M. M. Osman. Major Obstacles to Doxorubicin Therapy: Cardiotoxicity and Drug Resistance. *Journal of Oncology Pharmacy Practice*, 26(2):434–444, 2019. URL https://doi.org/10.1177/1078155219877931.

[34] H. J. Broxterman, K. J. Gotink, and H. M. W. Verheul. Understanding the Causes of Multidrug Resistance in Cancer: A Comparison of Doxorubicin and Sunitinib. *Drug Resistance Updates*, 12(4-5):114–126, 2009. URL https://doi.org/10.1016/j.drup.2009.07.00.

[35] G. Anandhakumari, P. Jayabal, A. Balasankar, T. H. Ramasundaram, S. Oh, K. Aruchamy, P. Kallem, and V. Polisetti. Synthesis of Strontium Oxide-Zinc Oxide Nanocomposites by Co-Precipitation Method and Its Application for Degradation of Malachite Green Dye under Direct Sunlight. *Heliyon*, 9(10):e20824, 2023. URL https://doi.org/10.1016/j.heliyon.2023.e20824.

[36] S.R. Ali, R. Kumar, A. Kalam, Al-Sehemi, A. G., and Mahesh Chandra Arya. Effect of Strontium Doping on the Band Gap of CeO_2 Nanoparticles Synthesized Using Facile Co-Precipitation. *Arabian journal for science and engineering*, 44(7):6295–6302, 2019. URL https://doi.org/10.1007/s13369-018-03700-x.

[37] M. L. Rahman, S. Rahman, B. Biswas, M. F. Ahmed, M. Rahman, and Nahid Sharmin. Investigation of Structural, Morphological and Magnetic Properties of Nanostructured Strontium Hexaferrite through Co-Precipitation Technique: Impacts of Annealing Temperature and Fe/Sr Ratio. *Heliyon*, 9(3):e14532, 2023. URL https://doi.org/10.1016/j.heliyon.2023.e14532.

[38] C.-F. Kao and C.-L. Jeng. Preparation and Characterisation of Lanthanum Nickel Strontium Oxides by Combined Coprecipitation and Molten Salt Reactions. *Ceramics International*, 26(3):237–243, 2000. URL https://doi.org/10.1016/s0272-8842(99)00048-6.

[39] P. Varadhan and M. Jayaraman. Hyalgan-Decorated-Ferulic Acid-Loaded Pullulan Acetate Nanoparticles against Gastrointestinal Cancer Cell Lines. *Emergent Materials*, 7(3):1115–1127, 2024. URL https://doi.org/10.1007/s42247-024-00634-z.

[40] R. Harun, A., S. Mishra, S. Pattnaik, and C. Mohanty. Berberine Loaded Glyceryl Monooleate Nanoparticles Exhibited Potent Intrinsic Anticancer Activity against Pancreatic Cancer Therapy: *In Vitro* and *in Silico* Studies. *Nano Trends*, 9:10009, 2025. URL https://doi.org/10.1016/j.nwnano.2025.100092.

[41] L. M. Lazer, Y. Kesavan, R. Gor, I. Ramachandran, S. Pathak, S. Narayan, M. Anbalagan, and S. Ramalingam. Targeting colon cancer stem cells using novel doublecortin like kinase 1 antibody functionalized folic acid conjugated hesperetin encapsulated chitosan nanoparticles. *Colloids and Surfaces B: Biointerfaces*, 217:112612, 2022.

[42] R. Salih, B. Khalid Bajou, Shaker, and Abdelaziz Elgamouz. Antitumor Effect of Algae Silver Nanoparticles on Human Triple Negative Breast Cancer Cells. *Biomedicine Pharmacotherapy*, 168:115532, 2023. URL https://doi.org/10.1016/j.biopha.2023.115532.

[43] C. R. Justus, N. Leffler, M. Ruiz-Echevarria, and L. V. Yang. *In Vitro* Cell Migration and Invasion Assays. *Journal of Visualized Experiments*, (88), 2014. URL https://doi.org/10.3791/51046.

[44] M. Roy, R. Pal, and A. S. Pelargonidin-PLGA Chakraborti. Pelargonidin-PLGA nanoparticles: Fabrication, characterization, and their effect on streptozotocin induced diabetic rats. *IJEB*, 5512:2017, December 2017. URL http://nopr.niscpr.res.in/handle/123456789/43234. [Accessed March 10, 2025].

[45] J. Junita, D. Jayalakshmi, and J.D. Rodney. Effect of Annealing Temperature on the Bifunctional Electrocatalytic Properties of Strontium Nickelate ($SrNiO_3$) Nanoparticles for Efficient Overall Water Splitting. *International Journal of Hydrogen Energy*, 47(71):30602–30612, 2022. URL https://doi.org/10.1016/j.ijhydene.2022.07.007.

[46] H. Lee, W.-H. Wu, B.-H. Chen, and J.-D. Liao. Heterogeneous Catalysts Using Strontium Oxide Agglomerates Depositing upon Titanium Plate for Enhancing Biodiesel Production. *Catalysts*, 11(1):30, 2020. URL https://doi.org/10.3390/catal11010030.

[47] H. Lin, Y.-H. She, B. R. Cassileth, F. Sirotnak, and S. Cunningham Rundles. Maitake Beta-Glucan MD-Fraction Enhances Bone Marrow Colony Formation and Reduces Doxorubicin Toxicity *in Vitro*. *International Immunopharmacology*, 4(1):91–99, 2004. URL https://doi.org/10.1016/j.intimp.2003.10.012.

[48] Neves A. B. Susana, J. J. Scott-Fordsmand, and B. Amorim. Reactive Oxygen Species Detection Using Fluorescence in Enchytraeus Crypticus—Method Implementation through Ag NM300K Case Study. *Toxics*, 9(10):232–232, 2021. URL https://doi.org/10.3390/toxics9100232.

[49] Shruti Sinnarkar, Poonam Suryawanshi, Amol Dilip, Jitendra Bhawalkar, and Vaibhav Ladke. Galangin Promotes Apoptosis by Upregulating the Pro-Apoptotic Gene BAX in Triple-Negative Breast Cancer. *Journal of the Egyptian National Cancer Institute*, 36(1), 2024. URL https://doi.org/10.1186/s43046-024-00246-y.

[50] K. W. Yip and J. C. Reed. Bcl-2 Family Proteins and Cancer. *Oncogene*, 27(50):6398–6406, 2008. URL https://doi.org/10.1038/onc.2008.307.

[51] T. Sanda, J. W. Tyner, A. Gutiérrez, V. N. Ngo, J. Glover, B. H. Chang, A. Yost, W. Ma, A. G. Fleischman, W. Zhou, Y. Yang, M. Kleppe, Y. Ahn, J. Tatarek, M. A. Kelliher, D. Neuberg, R. L. Levine, R. Moriggl, Gray Mathias Müller, and N. S. TYK2–STAT1–BCL2 Pathway Dependence in T-Cell Acute Lymphoblastic Leukemia. *Cancer Discovery*, 3(5):564–577, 2013. URL https://doi.org/10.1158/2159-8290.cd-12-0504.

[52] K. M. Boatright and G. S. Salvesen. Caspase Activation. *Biochemical Society Symposia*, 70:233–242, 2003. URL https://doi.org/10.1042/bss0700233.

[53] L. Zhang, C. Fang, X. Xu, A. Li, Q. Cai, and X. Long. Androgen Receptor, EGFR, and BRCA1 as Biomarkers in Triple-Negative Breast Cancer: A Meta-Analysis. *BioMed Research International*, 2015:1–12, 2015. URL https://doi.org/10.1155/2015/357485.

[54] G.I. Mun, E. Choi, H. Jin, S.-K. Choi, H. Lee, S. Kim, J. Kim, C. Kang, H. L. Oh, H.-J. Lee, D.-R. Ahn, and Y.-S. Lee. Phosphorylation of BRCA1 at serine 1387 plays a critical role in cathepsin S-mediated radiation resistance via BRCA1 degradation and BCL_2 stabilization. *Biochim. Biophys. Acta BBA - Mol. Basis Dis.*, 1871(1), 2025. URL https://doi.org/10.1016/j.bbadis.2024.167523. Article: 167523.